Article

Fabrication of Silver-Doped UiO-66-NH$_2$ and Characterization of Antibacterial Materials

Feng Tian [1]**, Rengui Weng** [1,]*****, Xin Huang** [1]**, Guohong Chen** [1] **and Zhitao Huang** [2]

1   College of Ecological Environment and Urban Construction, Fujian University of Technology, Fuzhou 350118, China
2   Sunstar Membrane Technology (Xiamen) Co., Ltd., Xiamen 361000, China
*   Correspondence: wengrengui109@fjut.edu.cn

Abstract: Metal-organic frameworks (MOFs) are highly crystalline inorganic-organic complexes formed from metal ions or metal clusters and multi-toothed organic ligands. MOFs have great potential for use in antibacterial materials in the biological, environmental, and food antimicrobial fields. They can act as a reservoir of metal ions, releasing them gradually and leading to a sustained antibacterial effect analogous to that proposed for metal oxide nanoparticles (NPs). Herein, UiO-66-NH$_2$ as a type of MOF was first prepared by a facile solvothermal method and then loaded with Ag NPs to form a Ag/UiO-66-NH$_2$ composite and the different materials were synthesized by controlling silver doping amount, which are then applied to an antibacterial test. Works on the synthesis of Ag/UiO-66-NH$_2$ and its antibacterial test were not reported before. The synthesized materials were characterized using the field emission scanning electron microscope (FE-SEM), X-ray diffractometer (XRD), Fourier transform infrared spectroscopy (FT-IR), Brunauer-Emmett-Teller (BET), thermal gravimetric analysis (TGA), and X-ray photoelectron spectroscopy (XPS) techniques. The antibacterial activity of the Ag/UiO-66-NH$_2$ was then assessed against *E. coli* (gram-negative bacteria) and Staphylococcus aureus (gram-positive bacteria), using the inhibition zone (ZIO) method and optical density (OD) method. The obtained results have shown that the introduction of Ag does not interfere with the crystallization of UiO-66-NH$_2$. The FT-IR spectral profiles recorded for the UiO-66-NH$_2$ samples fabricated under conditions of varying silver ion doping levels are similar to those recorded for UiO-66-NH$_2$. The thermal stability of UiO-66-NH$_2$ containing varying amounts of silver ions was lower than the thermal stability of UiO-66-NH$_2$. However, under these conditions, the specific surface area and pore volume increased. The antibacterial performance of UiO-66-NH$_2$ improved significantly following the process of silver ion doping. The best antibacterial performance was observed when the silver ion content was 4 wt.%. Overall, we synthesized a new nanocomposite material with broad-spectrum bacterial sterilization, which was easy to manufacture.

Keywords: silver; metal-organic frameworks; UiO-66-NH$_2$; antibacterial properties

1. Introduction

While the discovery and development of antibiotics undoubtedly provides effective ways to combat pathogens, the overuse of antibiotics leads to antimicrobial resistance [1–3]. Antibiotic resistance can develop through various mechanisms, including altering an antibiotic's target site or metabolic pathway, reducing the drug's accumulation in a cell, or inactivating it [4,5]. To this end, a new approach is required and there is an urgent need to develop effective antimicrobial materials. Both metal oxide nanoparticles (NPs) and metal-organic frameworks (MOFs) have shown remarkable antibacterial activity. Silver NPs (Ag NPs) are the most commonly applied in industry because of their unique biocidal features. The synthesis of Ag NPs is an important aspect of nanotechnology [6–8]. There are a wide variety of synthesis approaches because the physical, chemical, and biological properties are intensely dependent on the synthetic method. Generally, there are three

different categories on synthesizing Ag NPs, which are chemical, physical, and biological methods. The most common and widely reported synthesis method of Ag NPs is chemical reduction. Physical methods are generally fast and do not contain toxic or harmful chemicals. Nonetheless, the shortcoming of these methods is the high energy consumption required during the synthesis process [6,7,9–16]. Among nanomaterials with porous structures, MOFs appear promising because their active centers are an intrinsic part of the molecular structure, similar to those in NPs. Such centers are stabilized by forming chemical bonds which are extraordinarily strong to stabilize their form, but do not block their activity [17–19]. Producing Ag NPs without employing toxic reducing agents require biological methods, which are famous as green synthesis approaches [4,10,14]. Despite the benefits of green biological synthesis, controlling the polydispersity of NPs is a significant challenge. As a result, many strategies have been used to overcome these problems, among which immobilization of Ag NPs on different matrices has proven to be a more desired approach. MOFs as porous inorganic hybrids have usually been applied as models for the immobilization of metal oxide NPs [20–22].

MOFs are synthesized following the hydrothermal, solvothermal, solvent-free, and chemical vapor deposition methods, among which the simplest and most widely used method is hydrothermal synthesis [23–25]. MOFs are highly crystalline inorganic-organic complexes formed from metal ions or metal clusters and multi-toothed organic ligands [26,27]. MOFs have ultrahigh surface areas, porous structures, and most importantly, easy and uniform metal doping [28–31]. During the synthesis of MOFs, the site for metals can be replaced according to the need. A variety of metal ions, such as Cu^{2+}, Zn^{2+}, Ag^+, and Co^{2+} are easily loaded on MOFs, and most of them can act as chemical antibacterial agents [32]. Among all of the metal ions, the silver ion exhibits the strongest bactericidal ability. It also exhibits good antibacterial durability. These ions exhibit excellent performance at low dosages. The silver ions are highly stable and non-toxic, and they do not need to be stimulated before action. Therefore, silver ions can be efficiently used to modify MOF-based materials, which perform well in various fields. This method of tuning the characteristics of MOF-based materials can be potentially used for developing various materials in the future [33–36].

M.D. Firouzjaei et al. [37] reported a novel Ag-based nanocomposite (GO-Ag-MOF). They fabricated the material by modifying a silver (Ag) elemental organic framework (Ag-MOF) with graphene oxide (GO). They analyzed the growth curves and used fluorescence imaging and flow cytometry techniques to evaluate the toxicity of GO-Ag-MOF, Ag-MOF, and GO against *E. coli* (Gram-negative bacteria) and *Bacillus subtilis* (Gram-positive bacteria). The results revealed that GO-Ag-MOF exhibited significant antibacterial activity, and its biocidal activity was higher than that of Ag-MOF and GO-based nanomaterials. S.F. Seyedpour et al. [38] fabricated the material with silver as the center. The material was fabricated at room temperature using green solvents, following a simple and environmentally friendly method. Three new Ag-MOFs were fabricated, and the results from the experiments revealed that for silver and imidazole coupling agents under the Ag-MOFs, there was a synergistic action against *E. coli* in colloid form. Under these conditions, the bacterial death rate increased to 95% within 3 h. Zhang et al. [39] used Ag-Metal-organic framework-loaded chitosan NPs and polyvinyl alcohol/sodium alginate/chitosan as the upper and lower two layers to successfully synthesize a bilayer composite dressing for healing. Liu et al. [40] synthesized visible light-sensitive Ag/AgCl@ZIF-8 catalysts. After a series of characterizations of the material, they reached the results that the composite photo catalyst Ag/AgCl@ZIF-8 sample revealed exceptional photocatalytic antibacterial properties. Under light for 90 min, the composite material could inactivate almost all bacteria.

Consequently, MOFs are appropriate for the preparation of a nanoscale system with chemical antibacterial properties. Inspired by the works above, UiO-66-NH₂ as a kind of MOF is first synthesized by a hydrothermal synthesis method and then loaded with Ag NPs to form an Ag/UiO-66-NH₂ composite, and the different materials were synthesized by controlling the silver doping amount, which are applied to an antibacterial test. UiO-66-

NH$_2$ is a MOF with water stability, high heat resistance, and corrosion resistance. Due to the high specific area, large porosity, and chelation of the N atom and transition metal ions, UiO-66-NH$_2$ and its derivatives are widely used as adsorbents of transition metal ions [41–46]. Moreover, as far as we know, works on the synthesis of Ag/UiO-66-NH$_2$ and its antibacterial test were not reported before.

2. Experimental

2.1. Materials

Experimental instruments. The FA$_2$004B electronic balance was manufactured by the Shanghai Yueping Scientific Instrument Co., Ltd. (Shanghai, China). The TG18G type bench high-speed centrifuge was manufactured by the Gongyi Yuhua Instrument Co., Ltd. (Gongyi, Henan). The D8 X-ray diffractometer (XRD) was manufactured by Bruck AXS (Bruck, Germany). The JSM-7600f field emission scanning electron microscope (FE-SEM) was manufactured by the JEOL Company in Tokyo, Japan. The JEM-1400 transmission electron microscopy (TEM), the QUANTAX 400 element mapping (EDS), and the Nicolet-460 Fourier transform infrared (FT-IR) spectrometer were manufactured by Bruker, Bruker, Germany. The ASAP2020HD88 specific surface area and Brunauer-Emmett-Teller (BET) was manufactured by the Micromeritics Company (Shanghai, China) in the United States. The Q500 thermogravimetric analyzer (TGA) was manufactured by the TA Company (New Castle, DE, USA) in the United States. The AXISUlTRADLD X-ray electron spectrometer (XPS) was manufactured by the Shimadzu Company (Tokyo, Japan) in Japan. The software for processing images are Adobe Photoshop (PS) and Origin 2021. Data processing was done in Excel.

Reagents. Zirconium tetrachloride (ZrC1$_4$; analytically pure), 2-aminoterephthalic acid (2-BDC-NH$_2$; analytically pure), and *N,N*-dimethylformamide (DMF; analytically pure) were purchased from the Shanghai Aladdin Sublimation Technology Co., Ltd. (Shanghai, China). Methanol (analytically pure) and silver nitrate (AgNO$_3$; analytically pure) were purchased from the Nanjing Chemical Reagent Co., Ltd.. (Nanjing, China). Deionized water was produced in the laboratory.

2.2. Synthesis and Characterization of Ag/UiO-66-NH$_2$-Based Materials

Ag/UiO-66-NH$_2$ was synthesized following the solvothermal method. UiO-66-NH$_2$ was prepared according to a previous report [47–49]. Specifically, ZrC1$_4$ (0.772 g) and 2-BDC-NH$_2$ (0.556 g) was taken in 80 mL of DMF. Various concentrations of AgNO$_3$ (1%, 2%, 4%, and 6%; mass fraction of AgNO$_3$ calculated with respect to the amount of ZrC1$_4$ and 2-BDC-NH$_2$ taken together) were added to the solution successively, and the mixture was transferred to a stainless-steel high-pressure reaction kettle (100 mL) lined with Teflon and heated at 120 °C for 24 h. In the states of high pressure and high temperature, Ag NPs were mixed into a solution containing organic ligands. Afterwards, Ag NPs were absorbed on the MOF crystals. Thus a series of Ag/UiO-66-NH$_2$ compounds were obtained [50]. The product was cooled to room temperature and centrifuged at $4000 \times g$/min for 15 min to obtain the product as a yellow powder. The product was washed thrice with DMF and methanol. Following this, it was immersed in methanol (80 mL) and heated at 120 °C for 12 h. Subsequently, the sample was re-centrifuged, and the Ag/UiO-66-NH$_2$ system was dried in a vacuum oven at 120 °C for 12 h to obtain Ag/UIO-66-NH$_2$. The Ag and Ag/UiO-66-NH$_2$ are stable in water PBS and culture medium [51–54]. The products were recorded as UiO-66-NH$_2$ (A$_0$) 1 wt.% Ag/UiO-66-NH$_2$ (A$_1$), 2 wt.% Ag/UiO-66-NH$_2$ (A$_2$), 4 wt.% Ag/UiO-66-NH$_2$ (A$_3$), and 6 wt.% Ag/UiO-66-NH$_2$ (AA$_4$). Figure 1 is a flow chart that presents the method of preparation of the materials.
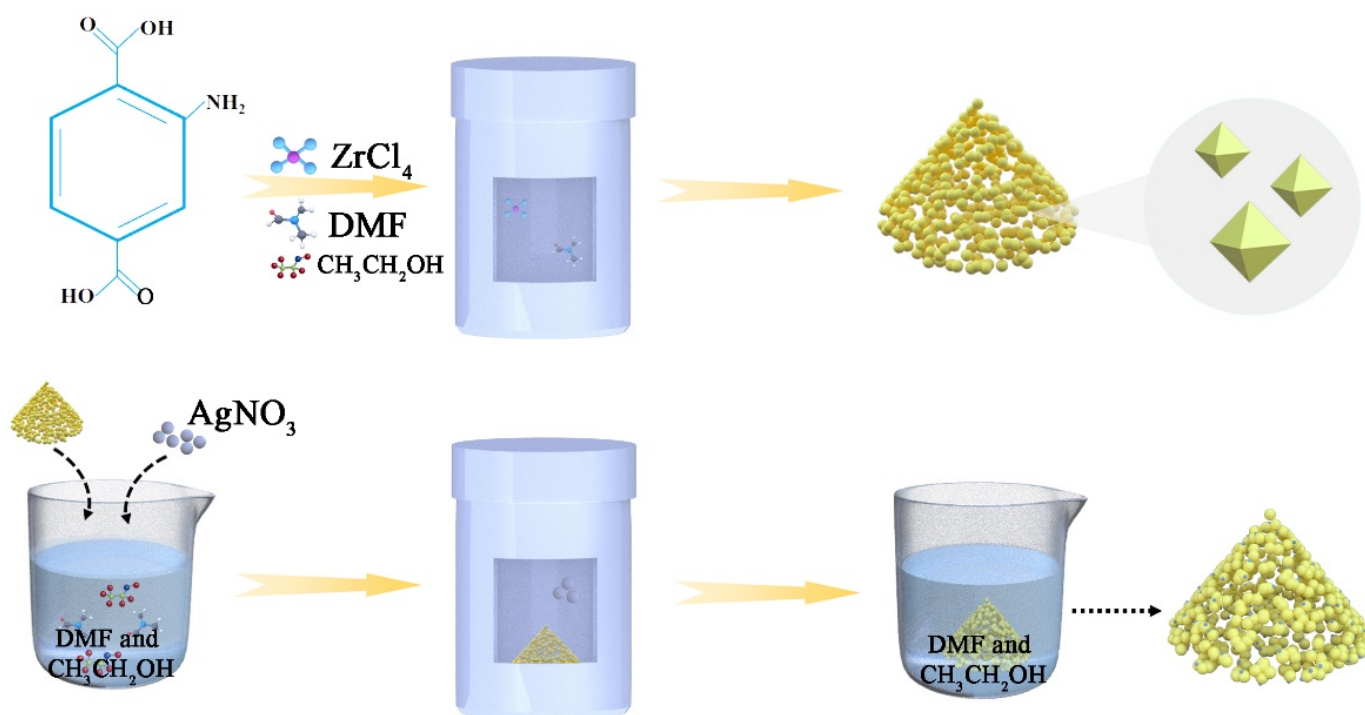
Figure 1. Flow chart presenting the method of material preparation.

The FE-SEM technique was used to observe the morphology of the samples, and high-resolution images of the sample were recorded. The tungsten filament was used as the light source, and the sample was amplified by 20,000 times under an acceleration voltage of 20 KV. The sample was sprayed with gold for 10 min before conducting the test [43]. The TEM was applied to inspect the surface structure of the samples at an accelerating voltage of 80 kV [50]. The XRD technique was used to analyze the crystal structure of the sample. The X-ray tube voltage was 40 kV, the current was 40 mA, and the Cu Kα ray was used for sample analysis at the scanning speed of 0.02/s. The 2θ test range was 5°–50°. The types, valence states, and composition of elements on the surface of samples were studied using the XPS technique [35,55]. The samples were put into the sample chamber of the XPS instrument. When the pressure in the sample chamber was under 2.0×10^{-7} Mbar, the sample was sent to the analysis chamber (spot size: 400 μm). The operating voltage was 12 kV, and the filament current was 6 mA. Full spectrum scanning energy was 150 eV, the step size was 1 eV, the narrow-spectrum scanning energy was 50 eV, and the step size was 0.1 eV [21].

The FT-IR technique was used to analyze the chemical composition of the sample. The sample was prepared under dry conditions. A small amount of the samples and a moderate amount of dry potassium bromide were placed in a mortar, and ground the sample into a powder. Subsequently, the ground sample was placed inside the tableting machine, and pressure was applied to the transparent slices. The background information was first collected, following which the infrared spectra were recorded (resolution: 4 cm^{-1}). The scanning number was 32, and the spectrum was recorded in the wave number range of 400–4000 cm^{-1}. The specific surface area, pore volume, and pore size distribution of the samples were determined by analyzing the BET isotherms. The BET equation was used to estimate the relative surface area, and the density functional theory (DFT) technique was used to determine the size of the aperture. The TGA technique was used to study the relationship between the mass and temperature of the samples to analyze the thermal stability of the samples. The samples were weighed and placed evenly in an alumina crucible in an atmosphere of nitrogen (nitrogen flow rate: 30 mL/min; heating rate: 10 °C/min). The testing range was in the range of room temperature to 800 °C [49,55–57].

3. Antibacterial Performance of the Ag/UiO-66-NH$_2$ Materials

The inhibition zone (ZIO) method was used to analyze the antibacterial activity of the Ag/UiO-66-NH$_2$. We chose *Staphylococcus aureus* (gram-positive strains, ATCC 6538) and *E. coli* (gram-negative, ATCC 25922). Firstly, we plated the bacterial suspension evenly on agar plates (Muller Hinton). In addition, sterile filter paper discs with a diameter of 6 mm were saturated with 35 μL nanocomposites and placed on solid medium. It was then incubated at 37 °C for 24 h and finally the inhibitory zone around each disc was measured in millimeters. At the intervals of 0 h, 1 h, 2 h, 3 h, 4 h, 5 h, and 6 h, 100 μL of the samples was taken out of the petri dishes. The Ultraviolet spectrophotometer was used to measure the optical density (OD) of the samples at a wavelength of 600 nm. The data were recorded, the growth curves corresponding to *E. coli* and *S. aureus* were generated, and the influence of different contact time on bacterial growth was observed.

4. Results and Discussion

4.1. SEM Analysis

SEM and TEM images (Figure 2A,C) demonstrated that synthesized UiO-66-NH$_2$ is an octahedral structure with a size of around 35 nm. After Ag NPs were deposited, the morphology of UiO-66-NH$_2$ hardly changed (Figure 2B). However, TEM images showed NPs on UiO-66-NH$_2$ particles (red circles in Figure 2D). EDS analysis revealed that these particles contained Ag (Figure 2E,F). In the EDS spectrum of UiO-66-NH$_2$, the corresponding peaks to the elements of Zr, O, C, and N appeared at 2.040, 0.526, 0.0.390, and 0.279, respectively. In addition, the EDS spectra of Ag/UiO-66-NH$_2$ showed a peak corresponding to Ag element at 3.012 (Figure 2F), which further confirms that Ag had been loaded on UiO-66-NH$_2$ successfully.
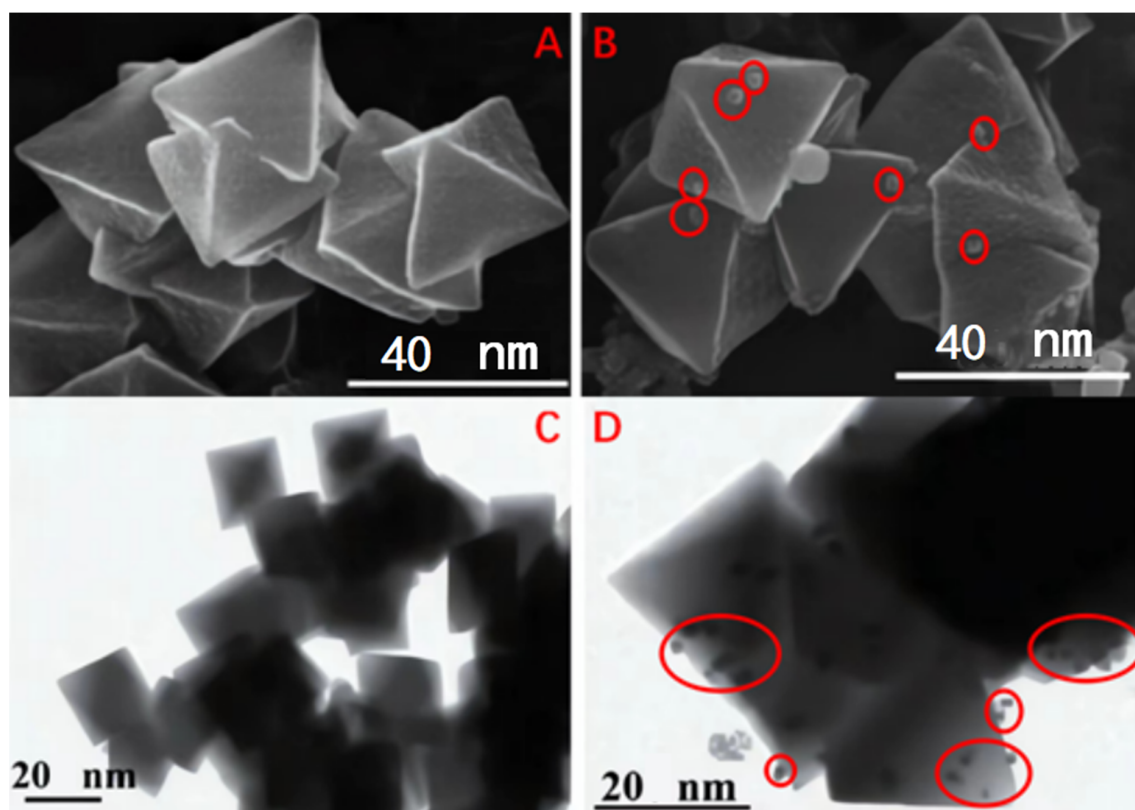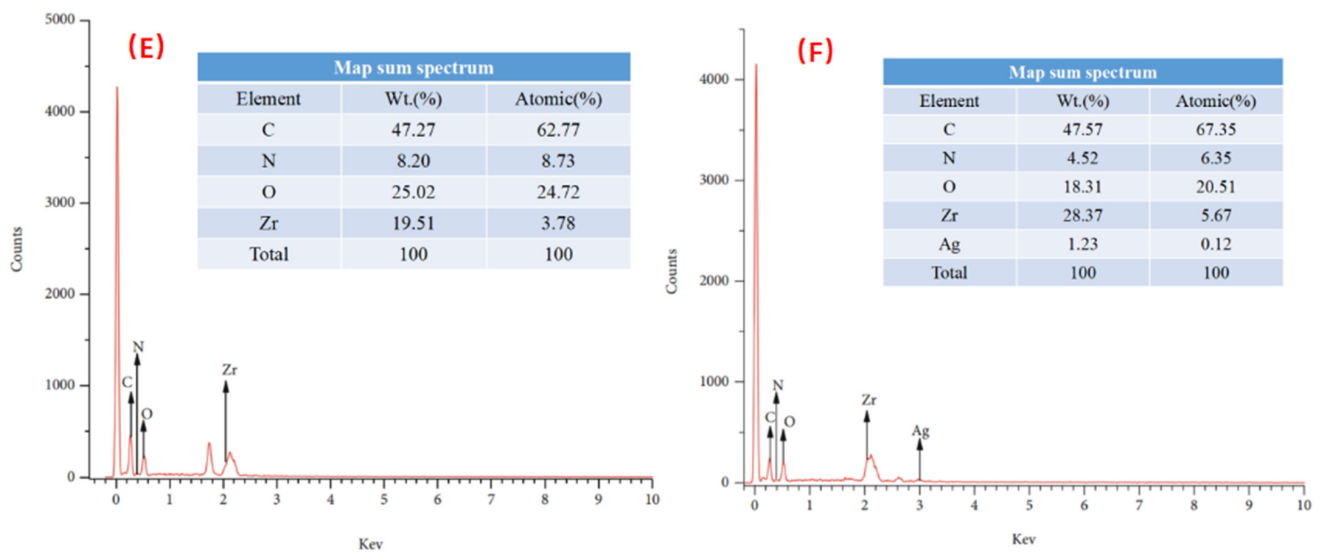

Figure 2. *Cont.*

Figure 2. (**A**,**C**) Field emission scanning electron microscope (FE-SEM) and transmission electron microscopy (TEM) images of UiO-66-NH$_2$; (**B**,**D**) SEM and TEM images of Ag/UiO-66-NH$_2$; (**E**,**F**) Element mapping (EDS) of UiO-66-NH$_2$ and Ag/UiO-66-NH$_2$.

4.2. XRD Analysis

Figure 3 presents the XRD patterns of UiO-66-NH$_2$ synthesized under conditions of varying silver doping levels. Typical strong diffraction peaks appear at 7.4°, 8.5°, 12.1°, 25.7°, and 33.1°, which represent the (111), (002), (022), (224), and (137) lattice planes of UiO-66-NH$_2$, respectively. The results agree well with the results reported by Lee D. T. et al. [58]. UiO-66-NH$_2$ was synthesized successfully. The positions of all of the peaks were the same, which indicated that the synthesized materials exhibited the same structure, and no obvious loss in crystal composition was observed. In addition, high intensities of the principal diffraction peaks were recorded. This indicated that the synthesized materials were characterized by good structural integrity and crystal properties. However, none of them showed the Ag-related diffraction peaks. It may be due to the poor crystallinity of Ag NPs [57].
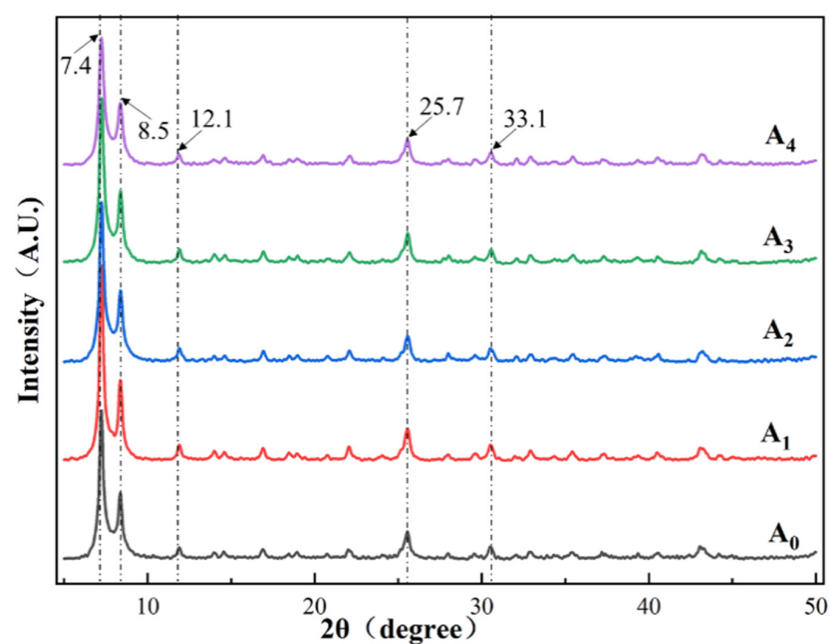

Figure 3. X-ray diffractometer (XRD) patterns of UiO-66-NH$_2$ synthesized under conditions of varying silver doping levels.

4.3. XPS Analysis

Figure 4 presents the full-spectrum XPS profile of UiO-66-NH$_2$ synthesized under conditions of varying silver doping levels. The peaks corresponding to Zr3d (193.98 eV), C1s (294.11 eV), N1s (399.98 eV), and O1s (544.98 eV) are clearly visible in the spectrograph. Significantly intense magazine peaks were not observed. Results obtained by conducting elemental analysis revealed that following the introduction of Ag, the intensity of the N1s peak associated with the C-NH$_2$ group decreased, indicating that N might react at this site [58]. The decrease in the intensity of the peaks corresponding to Zr3d and O1s indicates that the chemical environment of these two elements has changed. This phenomenon indicates that Zr-O participates in the reaction, and the O atom in the Zr-O-Zr structure potentially bonds with Ag through covalent bonds, resulting in a decrease in the binding energy of the O atom [33].
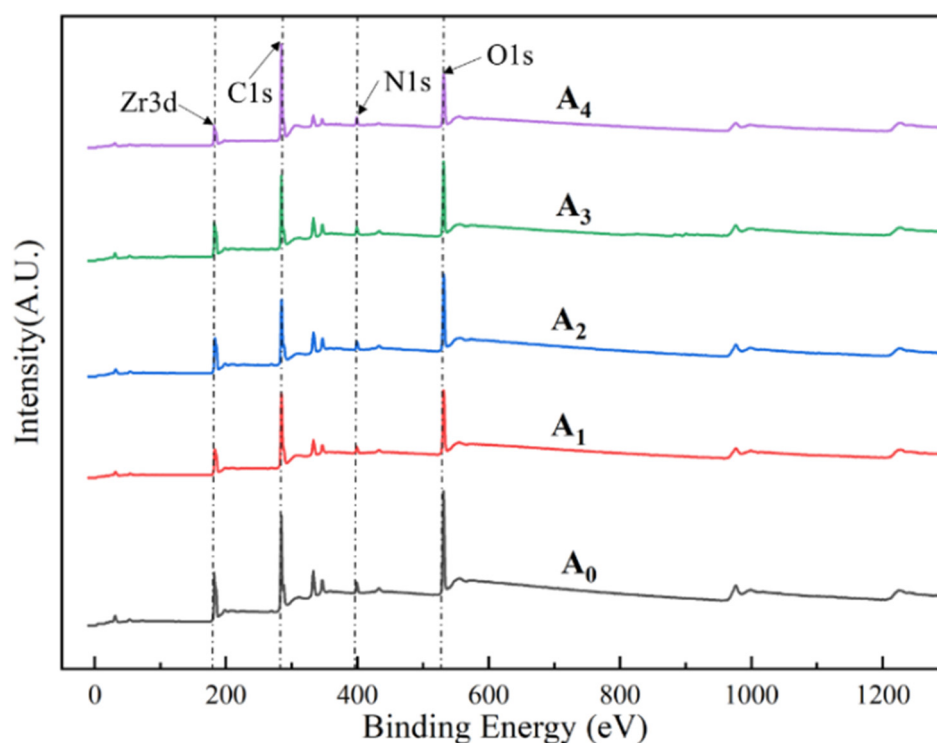

Figure 4. X-ray electron spectrometer (XPS) profiles of the UiO-66-NH$_2$ system synthesized under conditions of varying silver doping levels.

4.4. FT-IR Analysis

Figure 5 presents the FT-IR profile of the UiO-66-NH$_2$ system synthesized under conditions of varying silver doping levels. Analysis of the figure reveals that the peak at 3344 cm^{-1} is the characteristic peak of the OH group present on the surface of UiO-66-NH$_2$. The peak at 1655 cm^{-1} represents the bending vibration of the N-H group present in UiO-66-NH$_2$. The peaks at 1572 and 1386 cm^{-1} correspond to the symmetric and asymmetric stretching vibrations, respectively, of the COO group connected to Zr^{4+} in UiO-66-NH$_2$. The peak at 1499 cm^{-1} represents the stretching vibration of the C=C unit present in the benzene ring. The peak at 1434 cm^{-1} can be attributed to the shear vibration peak of the N-H unit in UiO-66-NH$_2$. The peak at 1256 cm^{-1} can be attributed to the unique C-N tensile absorption of aromatic amines. The peaks at 768 and 662 cm^{-1} represent the stretching vibration of μ3-O in Zr-(OC). The peak at the range 600 to 483 cm^{-1} is attributed to the metal-oxide bonds in the secondary construction unit [56]. Thus, it could be further inferred that UiO-66-NH$_2$ was successfully synthesized, and the peaks in the infrared spectral profiles recorded for A$_1$, A$_2$, A$_3$, and A$_4$ were similar to those appearing in the profiles recorded for UiO-66-NH$_2$. This validated that the crystal structure of Ag/UiO-66-NH$_2$ was stable.
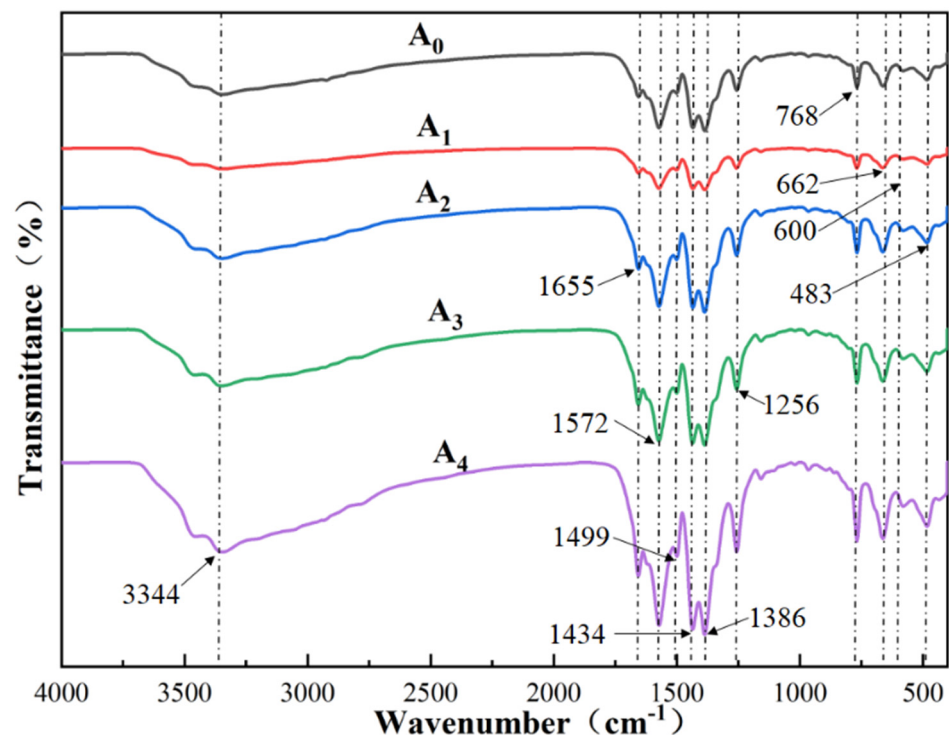
Figure 5. Fourier transform infrared (FT-IR) profiles recorded for UiO-66-NH$_2$ synthesized under conditions of varying silver doping levels.

4.5. BET Analysis

Figure 6 presents the nitrogen adsorption/desorption isotherms of the UiO-66-NH$_2$ system synthesized under conditions of varying silver doping levels. Type I isotherms were generated for all the synthesized materials. This indicated that they primarily presented microporous structures. As micropore filling is observed in type I isotherms, it is situated at a low relative pressure region. The adsorption capacity increases rapidly and reaches a plateau when the limit is reached. The specific surface area and total pore volume of A$_0$–A$_4$ are shown in Table 1. The specific surface area of UiO-66-NH$_2$ is slightly smaller than that reported [55] previously. This can be attributed to the fact that the amount of DMF used influences the dosage ratio of Zr in the synthesis process. The specific surface area and total pore volume of Ag/UiO-66-NH$_2$ are larger than those of UiO-66-NH$_2$, indicating that the introduction of Ag exerts no adverse effect on the original void structure of UiO-66-NH$_2$. Under these conditions, new pores are generated on the composite interface.

Table 1. Porous structure parameters of different samples.

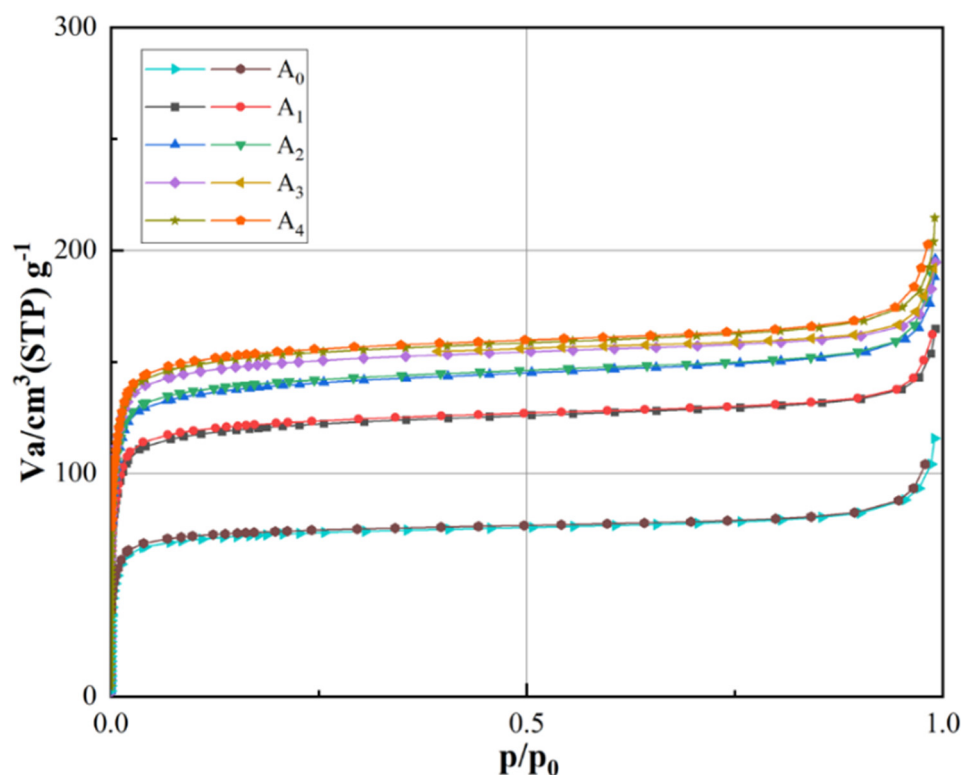| Sample Name	Specific Surface Area (m^2/g)	Total Pore Volume (m^3/g)
A$_0$	462.96	0.16
A$_1$	465.25	0.16
A$_2$	527.74	0.18
A$_3$	574.93	0.20
A$_4$	741.60	0.27

Figure 6. Nitrogen adsorption/desorption isotherms generated for the UiO-66-NH$_2$ system synthesized under conditions of varying silver doping levels.

4.6. TGA Analysis

Figure 7 presents the TGA profile of UiO-66-NH$_2$ synthesized under conditions of varying silver doping levels. As shown in the figure, the weight loss process associated with A$_0$–A$_4$ is divided into three stages. The first stage of weight loss, associated with A$_0$–A$_4$, occurs below 160 °C, and the mass losses for A$_0$–A$_4$ at this stage are 8.55%, 9.39%, 9.97%, 9.98%, and 11.10%, respectively. This can be primarily attributed to the evaporation of the gaseous products. The process is mediated through the physical adsorption of water molecules, DMF, and other solvents. The second stage of weight loss occurred in the range of 160 °C–580 °C, and the mass loss percentages were 31.12%, 31.88%, 31.93%, 32.32%, and 32.81%. This can be primarily attributed to the fact that as the amino terbenzoic acid ligand starts to decompose, the coordination bond with Zr breaks, and the skeleton structure gradually collapses under these conditions. In the third stage of weight loss, beyond 580 °C, the mass loss is approximately 8.3%. At this point, complete decomposition occurs, and the rate of decomposition decreases and gradually reaches a constant value. A similar extent of mass loss was observed for these materials. This indicated that the introduction of the Ag ions on UiO-66-NH$_2$ does not affect the thermal stability of the system. Good thermal stability could be achieved [47,49,59].
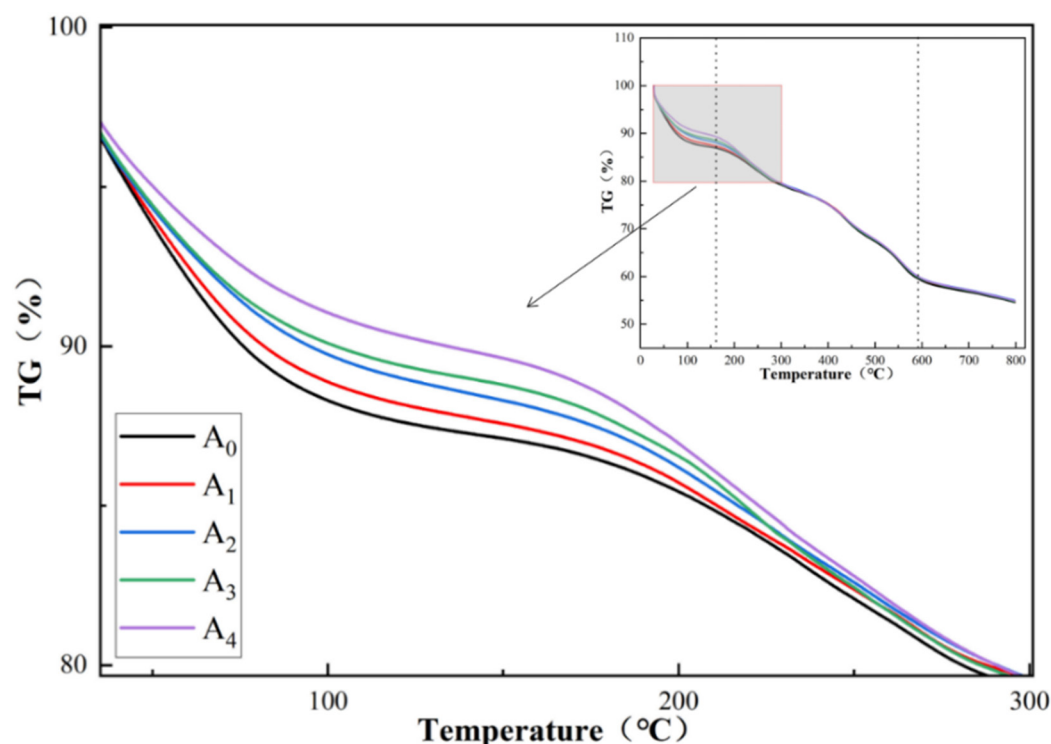
Figure 7. Thermogravimetric analyzer (TGA) profile recorded for the UiO-66-NH$_2$ system synthesized under conditions of varying silver doping levels.

5. Evaluation of the Antibacterial Performance

5.1. Inhibition Zone (ZOI)

The bacteriostatic zone method is one of the important methods that can be used to study the antibacterial properties of materials. The larger the diameter of the bacteriostatic zone is, the better the antibacterial effect and antibacterial performance of the material is.

We weighed 100 mg of the composite materials and pressed them into discs with molds. Subsequently, we placed the discs gently into a solid culture medium coated with bacterial suspension. The samples were then sealed with paraffin wax and incubated in a constant temperature oscillation chamber for 24 h under appropriate conditions. The diameter D of the circle was measured using a measuring scale. The results are presented in Figures 8 and 9, and Table 2.

Sample A$_0$ presented in Figure 8 exhibits almost no antibacterial properties, while A$_1$–A$_4$ exhibit different degrees of antibacterial properties. Analysis of the antibacterial zone diameter presented in Histogram Figure 8, Table 1, and other experimental data reveal that the degree of antibacterial effect that Ag/UiO-66-NH$_2$ exerted on *Staphylococcus aureus* is higher than the degree of the antibacterial effect exerted on *Escherichia coli*. It was also observed that the antibacterial zone diameter of 4 wt.% Ag/UiO-66-NH$_2$ for *Escherichia coli* was 7.452 mm. The antibacterial zone diameter corresponding to *Staphylococcus aureus* was 9.013 mm. These were the maximum diameters that were recorded under the same experimental conditions. Therefore, 4 wt.% Ag/UiO-66-NH$_2$ exhibited the best antibacterial effect. The antibacterial effect decreased with an increase in the silver doping amount. The generation of the change can be attributed to the gradual increase in the amount of Ag, which coalesce to form large silver particles. These are characterized by poor dispersion ability and low activity. A slow release of silver ions is achieved under the reaction conditions, resulting in the deterioration in the antibacterial performance of the sample [21,60–62]. It can be seen from the figure that the material exhibits good antibacterial activity against two representative bacteria, namely, *E. coli* (gram-negative bacteria) and *Staphylococcus aureus* (gram-positive bacteria), indicating that the material is a broad-spectrum antibacterial material.
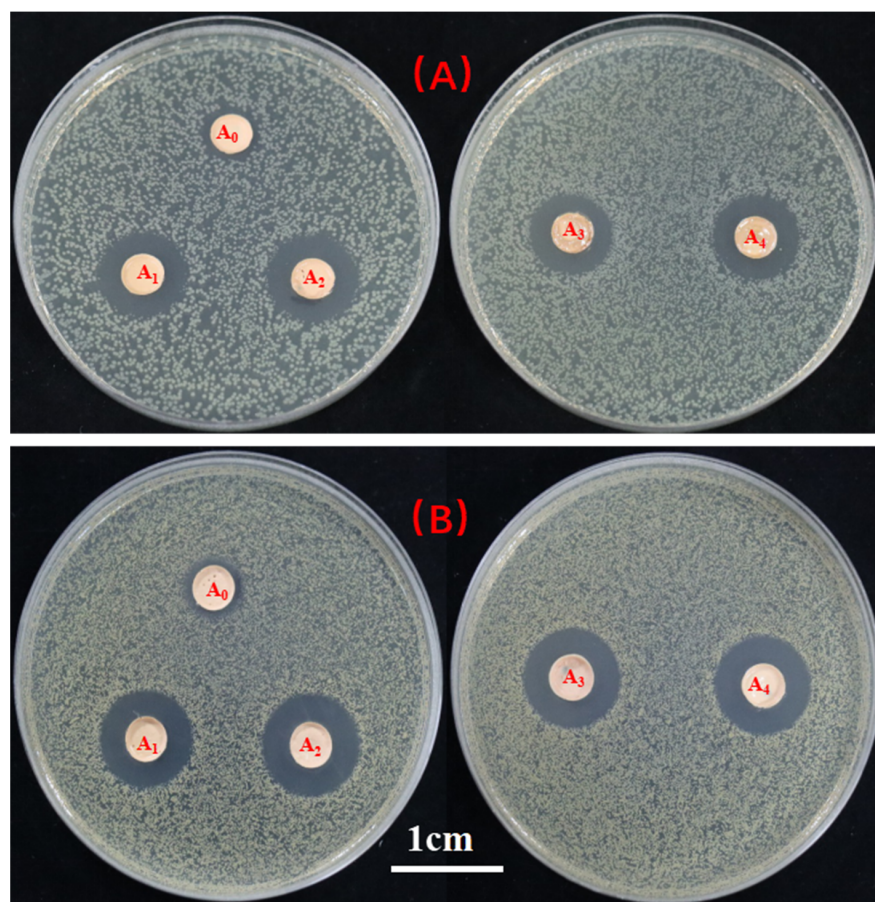
Figure 8. (**A**) A_0–A_4 image of the inhibition zone in *Escherichia coli* and (**B**) A_0–A_4 image of the inhibition zone in *Staphylococcus aureus*.
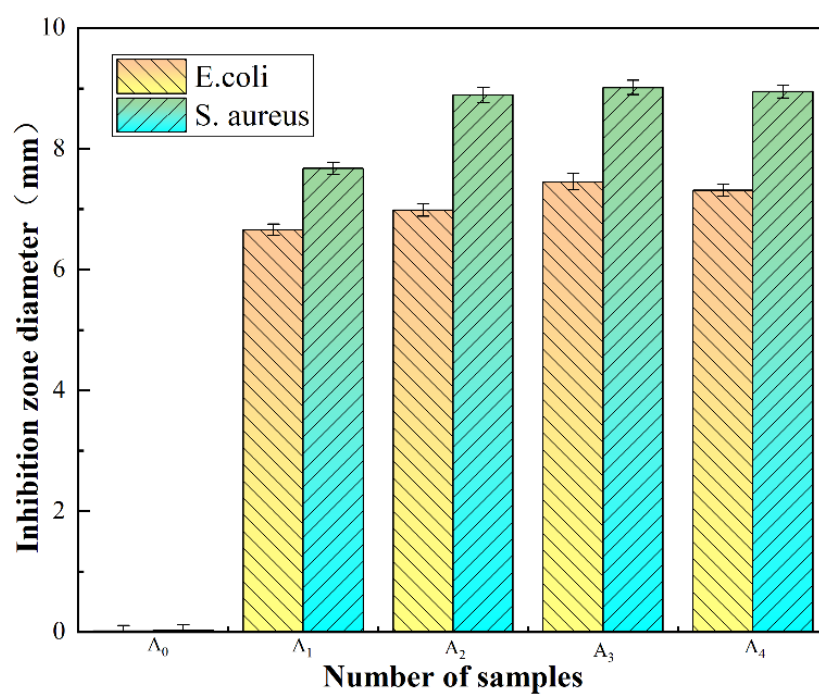

Figure 9. Diameters of the antibacterial circles corresponding to *Escherichia coli* and *Staphylococcus aureus* generated under conditions of varying silver doping levels.

Table 2. The average and standard Deviation of Diameter of the inhibition zone D (mm) corresponding to Ag/UiO-66-NH$_2$ under conditions of varying silver doping levels.

		A$_0$	A$_1$	A$_2$	A$_3$	A$_4$
E. coli	Average	0.017	6.658	6.985	7.453	7.312
	Standard Deviation	8.16×10^{-4}	6.53×10^{-3}	2.36×10^{-3}	1.41×10^{-3}	9.43×10^{-4}
S. aureus	Average	0.025	7.674	8.892	9.013	8.947
	Standard Deviation	4.08×10^{-3}	3.27×10^{-3}	1.63×10^{-3}	2.45×10^{-3}	5.72×10^{-3}

5.2. Determination of the Bacterial Growth Curve

The growth curves of two kinds of bacteria were generated following the addition of antibacterial materials to better understand the antibacterial performance of Ag/UiO-66-NH$_2$ under conditions of varying silver doping levels. Results obtained by conducting preliminary experiments revealed that at the Ag/UiO-66-NH$_2$ concentrations of 0.33 mg/L (50 mg/150 mL) and 0.27 mg/L (40 mg/150 mL), bacteria did not grow. The growth inhibition effect of different silver dosage levels of Ag/UiO-66-NH$_2$ on the growth properties of *Escherichia coli* and *Staphylococcus aureus* were studied. The optimized conditions have been reported: The Ag/UiO-66-NH$_2$ composites (30 mg) containing different silver dosage levels were dissolved in 150 mL of the fresh LB liquid medium to prepare the liquid medium (0.2 mg/L) containing antibacterial materials.

Figure 10 presents the curves corresponding to the growth of *Escherichia coli* and *Staphylococcus aureus*. The curves were generated following the addition of the antibacterial materials into the bacterial culture medium. The silver doping levels were varied to study the inhibition effect. Silver NPs can damage the phospholipid bilayer and permeability of cell membranes, causing the leakage of sugars and proteins in bacterial cells. Thus, cell death was induced [61,62]. As can be seen from Figures 10 and 11, 4 wt.% Ag/UiO-66-NH$_2$ exerts the strongest inhibitory effect on the growth of the two kinds of bacteria, and the OD values measured at the sixth hour are the lowest. This is consistent with the experimental results obtained by analyzing the bacteriostatic zone.
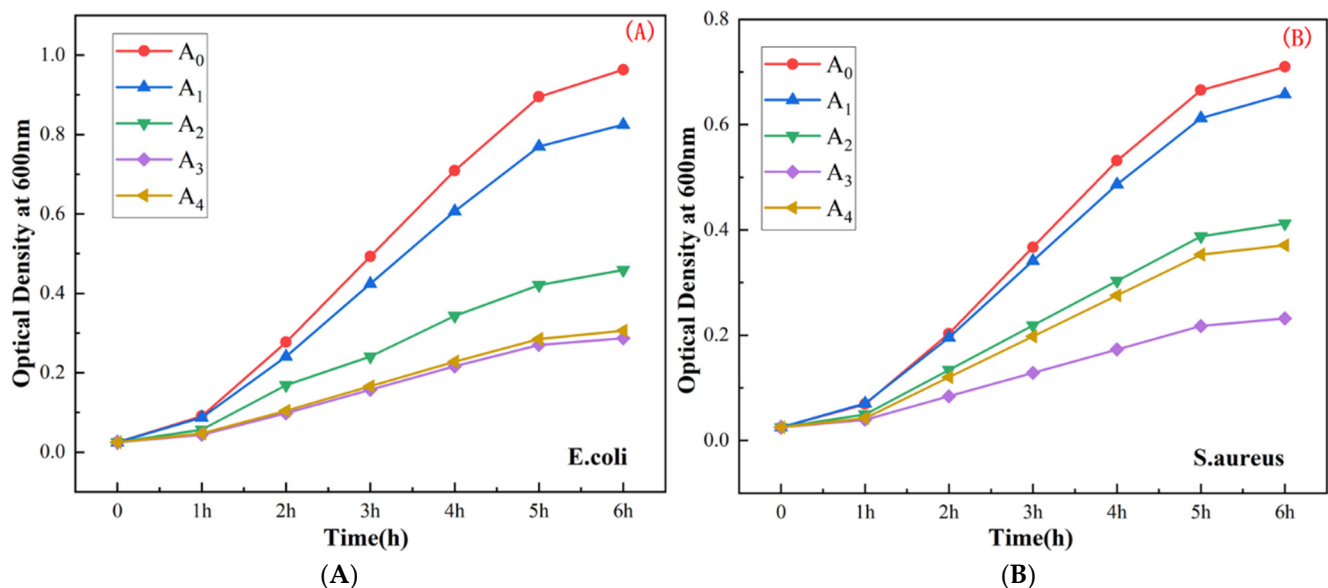
Figure 10. Growth curves for (**A**) *E. coli* and (**B**) *S. aureus*.
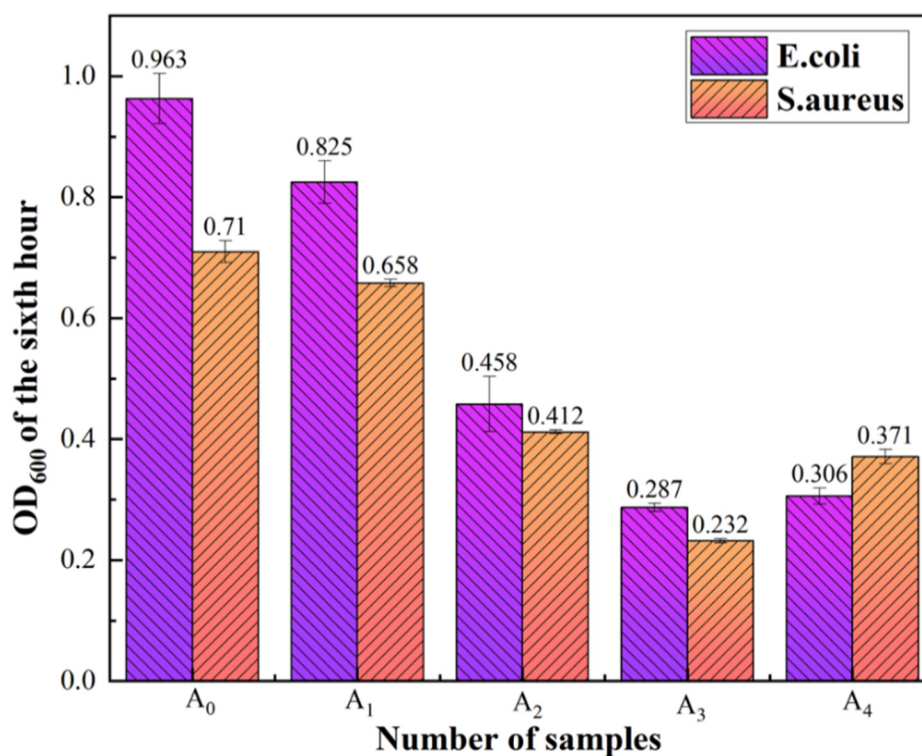
Figure 11. Final optical density for *E. coli* and *S. aureus*.

6. Conclusions

In this paper, UiO-66-NH$_2$, 1 wt.% Ag/UiO-66-NH$_2$, 2 wt.% Ag/UiO-66-NH$_2$, 4 wt.% Ag/UiO-66-NH$_2$, and 6 wt.% Ag/UiO-66-NH$_2$ were synthesized following the thermal solvent method. FE-SEM, XRD, FT-IR, BET, TGA, and XPS techniques were used to characterize the synthesized materials. The antibacterial properties were tested by analyzing ZIO and the OD values. The conclusions drawn follow:

(1) The introduction of Ag does not interfere with the crystallization of UiO-66-NH$_2$. The morphology and crystal structure of the UiO-66-NH$_2$ samples fabricated under conditions of varying silver ion doping levels amount are similar to those of UiO-66-NH$_2$.

(2) The FT-IR spectral profiles recorded for the UiO-66-NH$_2$ samples fabricated under conditions of varying silver ion doping levels are similar to those recorded for UiO-66-NH$_2$. Stray peaks were not observed, and the peak intensity decreased slightly.

(3) The thermal stability of UiO-66-NH$_2$, containing varying amounts of silver ions, was lower than the thermal stability of UiO-66-NH$_2$. The higher the silver ion content, the lower the thermal stability. Under these conditions, the specific surface area and pore volume increased.

(4) The antibacterial performance of UiO-66-NH$_2$ improved significantly following the process of silver ion doping. As the silver ion content increased, the antibacterial performance improved initially and then deteriorated. The best antibacterial performance was observed when the silver ion content was 4 wt.%.

Overall, Ag loading improves the antibacterial properties of UiO-66-NH$_2$. The preparation process of this material is simple, which provides the idea for the preparation of other composite materials. This research also contributes to the understanding of the role of loaded metal NPs and provides new strategies for broad-spectrum bacterial sterilization in many biological applications.

Author Contributions: F.T.: Methodology, Investigation, Writing—Original draft, Data curation, Visualization, and Supervision. R.W.: Supervision, Writing—Reviewing and Editing, Project adminis-

tration, and Funding acquisition. X.H. and G.C.: Investigation and Data curation. Z.H.: Supervision and Writing-Reviewing. All authors have read and agreed to the published version of the manuscript.

Institutional Review Board Statement: Not applicable.

Informed Consent Statement: Not applicable.

Data Availability Statement: The data presented in this study are available on request from the corresponding author.

Conflicts of Interest: The authors declare no conflict of interest.

References

1. Cook, M.A.; Wright, G.D. The past, present, and future of antibiotics. *Sci. Transl. Med.* **2022**, *14*, eabo7793. [CrossRef] [PubMed]
2. Nanayakkara, A.K.; Boucher, H.W.; Fowler, V.G., Jr.; Jezek, A.; Outterson, K.; Greenberg, D.E. Antibiotic resistance in the patient with cancer: Escalating challenges and paths forward. *CA Cancer J. Clin.* **2021**, *71*, 488–504. [CrossRef] [PubMed]
3. Chinemerem Nwobodo, D.; Ugwu, M.C.; Oliseloke Anie, C.; Al-Ouqaili, M.T.S.; Chinedu Ikem, J.; Victor Chigozie, U.; Saki, M. Antibiotic resistance: The challenges and some emerging strategies for tackling a global menace. *J. Clin. Lab. Anal.* **2022**, *36*, e24655. [CrossRef] [PubMed]
4. Samreen Ahmad, I.; Malak, H.A.; Abulreesh, H.H. Environmental antimicrobial resistance and its drivers: A potential threat to public health. *J. Glob. Antimicrob. Resist.* **2021**, *27*, 101–111. [CrossRef] [PubMed]
5. Razzaque, M.S. Commentary: Microbial Resistance Movements: An Overview of Global Public Health Threats Posed by Antimicrobial Resistance, and How Best to Counter. *Front. Public Health* **2020**, *8*, 629120. [CrossRef]
6. Ocsoy, I.; Gulbakan, B.; Chen, T.; Zhu, G.; Chen, Z.; Sari, M.M.; Peng, L.; Xiong, X.; Fang, X.; Tan, W. DNA-guided metal-nanoparticle formation on graphene oxide surface. *Adv. Mater.* **2013**, *25*, 2319–2325. [CrossRef]
7. Ocsoy, I.; Paret, M.L.; Ocsoy, M.A.; Kunwar, S.; Chen, T.; You, M.; Tan, W. Nanotechnology in plant disease management: DNA-directed silver nanoparticles on graphene oxide as an antibacterial against Xanthomonas perforans. *ACS Nano* **2013**, *7*, 8972–8980. [CrossRef]
8. Nakamura, S.; Sato, M.; Sato, Y.; Ando, N.; Takayama, T.; Fujita, M.; Ishihara, M. Synthesis and Application of Silver Nanoparticles (Ag NPs) for the Prevention of Infection in Healthcare Workers. *Int. J. Mol. Sci.* **2019**, *20*, 3620. [CrossRef]
9. Kalaivani, R.; Maruthupandy, M.; Muneeswaran, T.; Hameedha Beevi, A.; Anand, M.; Ramakritinan, C.M.; Kumaraguru, A.K. Synthesis of chitosan mediated silver nanoparticles (Ag NPs) for potential antimicrobial applications. *Front. Lab. Med.* **2018**, *2*, 30–35. [CrossRef]
10. Hawar, S.N.; Al-Shmgani, H.S.; Al-Kubaisi, Z.A.; Sulaiman, G.M.; Dewir, Y.H.; Rikisahedew, J.J.; Omri, A. Green Synthesis of Silver Nanoparticles from Alhagi graecorum Leaf Extract and Evaluation of Their Cytotoxicity and Antifungal Activity. *J. Nanomater.* **2022**, *2022*, 1058119. [CrossRef]
11. Al Rugaie, O.; Jabir, M.S.; Mohammed, M.K.A.; Abbas, R.H.; Ahmed, D.S.; Sulaiman, G.M.; Mohammed, S.A.A.; Khan, R.A.; Al-Regaiey, K.A.; Alsharidah, M.; et al. Modification of SWCNTs with hybrid materials ZnO-Ag and ZnO-Au for enhancing bactericidal activity of phagocytic cells against Escherichia coli through NOX2 pathway. *Sci. Rep.* **2022**, *12*, 17203. [CrossRef] [PubMed]
12. Ibraheem, D.R.; Hussein, N.N.; Sulaiman, G.M.; Mohammed, H.A.; Khan, R.A.; Al Rugaie, O. Ciprofloxacin-Loaded Silver Nanoparticles as Potent Nano-Antibiotics against Resistant Pathogenic Bacteria. *Nanomaterials* **2022**, *12*, 2808. [CrossRef]
13. Dam, P.; Altuntas, S.; Mondal, R.; Baudrit, J.R.V.; Kati, A.; Ghorai, S.; Sadat, A.; Gangopadhyay, D.; Shaw, S.; Franco, O.L.; et al. Silk-based nano-biocomposite scaffolds for skin organogenesis. *Mater. Lett.* **2022**, *327*, 133024. [CrossRef]
14. Khane, Y.; Benouis, K.; Albukhaty, S.; Sulaiman, G.M.; Abomughaid, M.M.; Al Ali, A.; Aouf, D.; Fenniche, F.; Khane, S.; Chaibi, W.; et al. Green Synthesis of Silver Nanoparticles Using Aqueous Citrus limon Zest Extract: Characterization and Evaluation of Their Antioxidant and Antimicrobial Properties. *Nanomaterials* **2022**, *12*, 2013. [CrossRef]
15. Strayer, A.; Ocsoy, I.; Tan, W.; Jones, J.B.; Paret, M.L. Low Concentrations of a Silver-Based Nanocomposite to Manage Bacterial Spot of Tomato in the Greenhouse. *Plant Dis.* **2016**, *100*, 1460–1465. [CrossRef]
16. Leng, Y.; Fu, L.; Ye, L.; Li, B.; Xu, X.; Xing, X.; He, J.; Song, Y.; Leng, C.; Guo, Y.; et al. Protein-directed synthesis of highly monodispersed, spherical gold nanoparticles and their applications in multidimensional sensing. *Sci. Rep.* **2016**, *6*, 28900. [CrossRef] [PubMed]
17. Duan, C.; Liu, C.; Meng, X.; Lu, W.; Ni, Y. Fabrication of carboxymethylated cellulose fibers supporting Ag NPs@MOF-199s nanocatalysts for catalytic reduction of 4-nitrophenol. *Appl. Organomet. Chem.* **2019**, *33*, e4865. [CrossRef]

18. Mukoyoshi, M.; Kobayashi, H.; Kusada, K.; Hayashi, M.; Yamada, T.; Maesato, M.; Taylor, J.M.; Kubota, Y.; Kato, K.; Takata, M.; et al. Hybrid materials of Ni NP@MOF prepared by a simple synthetic method. *Chem. Commun.* **2015**, *51*, 12463–12466. [CrossRef]

19. Dai, S.; Ngoc, K.P.; Grimaud, L.; Zhang, S.; Tissot, A.; Serre, C. Impact of capping agent removal from Au NPs@MOF core-shell nanoparticle heterogeneous catalysts. *J. Mater. Chem. A* **2022**, *10*, 3201–3205. [CrossRef]

20. Cai, G.; Yan, P.; Zhang, L.; Zhou, H.C.; Jiang, H.L. Metal-Organic Framework-Based Hierarchically Porous Materials: Synthesis and Applications. *Chem. Rev.* **2021**, *121*, 12278–12326. [CrossRef]

21. Sacourbaravi, R.; Ansari-Asl, Z.; Kooti, M.; Nobakht, V.; Darabpour, E. Fabrication of Ag NPs/Zn-MOF Nanocomposites and Their Application as Antibacterial Agents. *J. Inorg. Organomet. Polym. Mater.* **2020**, *30*, 4615–4621. [CrossRef]

22. Zheng, L.; Wang, F.; Jiang, C.; Ye, S.; Tong, J.; Dramou, P.; He, H. Recent progress in the construction and applications of metal-organic frameworks and covalent-organic frameworks-based nanozymes. *Coord. Chem. Rev.* **2022**, *471*, 214760. [CrossRef]

23. Jiang, Z.; Xue, W.; Huang, H.; Zhu, H.; Sun, Y.; Zhong, C. Mechanochemistry-assisted linker exchange of metal-organic framework for efficient kinetic separation of propene and propane. *Chem. Eng. J.* **2023**, *454*, 140093. [CrossRef]

24. Lin, Y.; Su, P.; Li, W. Chemical vapor deposition of guest-host dual metal-organic framework heterosystems for high-performance mixed matrix membranes. *Appl. Mater. Today* **2022**, *27*, 101462. [CrossRef]

25. Wang, Z.; Hou, X.; Dekyvere, S.; Mousavi, B.; Chaemchuen, S. Single-thermal synthesis of bimetallic Co/Zn@NC under solvent-free conditions as an efficient dual-functional oxygen electrocatalyst in Zn-air batteries. *Nanoscale* **2022**, *14*, 16683–16694. [CrossRef]

26. Moharramnejad, M.; Ehsani, A.; Salmani, S.; Shahi, M.; Malekshah, R.E.; Robatjazi, Z.S.; Parsimehr, H. Zinc-based metal-organic frameworks: Synthesis and recent progress in biomedical application. *J. Inorg. Organomet. Polym. Mater.* **2022**, *32*, 3339–3354. [CrossRef]

27. Zhang, Q.; Yang, H.; Zhou, T.; Chen, X.; Li, W.; Pang, H. Metal-Organic Frameworks and Their Composites for Environmental Applications. *Adv. Sci.* **2022**, *9*, e2204141. [CrossRef]

28. Yang, G.; Liu, J.; Zhou, M.; Bai, J.; Bo, X. Fast and Facile Room-Temperature Synthesis of MOF-Derived Co Nanoparticle/Nitrogen-Doped Porous Graphene in Air Atmosphere for Overall Water Splitting. *ACS Sustain. Chem. Eng.* **2020**, *8*, 11947–11955. [CrossRef]

29. Wu, Y.; Huang, Z.; Jiang, H.; Wang, C.; Zhou, Y.; Shen, W.; Xu, H.; Deng, H. Facile Synthesis of Uniform Metal Carbide Nanoparticles from Metal-Organic Frameworks by Laser Metallurgy. *ACS Appl. Mater. Interfaces* **2019**, *11*, 44573–44581. [CrossRef]

30. Qiu, J.-L.; Su, J.; Muhammad, N.; Zheng, W.T.; Yue, C.-L.; Liu, F.-Q.; Zuo, J.-L.; Ding, Z.-J. Facile encapsulating Ag nanoparticles into a Tetrathiafulvalene-based Zr-MOF for enhanced Photocatalysis. *Chem. Eng. J.* **2022**, *427*, 131970. [CrossRef]

31. Bereketova, A.; Nallal, M.; Yusuf, M.; Jang, S.; Selvam, K.; Park, K.H. A Co-MOF-derived flower-like CoS@S,N-doped carbon matrix for highly efficient overall water splitting. *RSC Adv.* **2021**, *11*, 16823–16833. [CrossRef] [PubMed]

32. Peng, P.; Zhao, C.; Ji, J.; Chen, W.; Ding, N.; Li, S.; Pang, S. Simple and selective method for simultaneous removal of mercury(ii) and recovery of silver(i) from aqueous media by organic ligand 4,4′-azo-1,2,4-triazole. *Environ. Sci. Water Res. Technol.* **2022**, *8*, 534–542. [CrossRef]

33. Liu, Y.; Zhou, L.; Dong, Y.; Wang, R.; Pan, Y.; Zhuang, S.; Liu, D.; Liu, J. Recent developments on MOF-based platforms for antibacterial therapy. *RSC Med. Chem.* **2021**, *12*, 915–928. [CrossRef] [PubMed]

34. Li, X.; Zhao, X.; Chu, D.; Zhu, X.; Xue, B.; Chen, H.; Zhou, Z.; Li, J. Silver nanoparticle-decorated 2D Co-TCPP MOF nanosheets for synergistic photodynamic and silver ion antibacterial. *Surf. Interfaces* **2022**, *33*, 128524. [CrossRef]

35. Zheng, H.; Wang, D.; Sun, X.; Jiang, S.; Liu, Y.; Zhang, D.; Zhang, L. Surface modified by green synthetic of Cu-MOF-74 to improve the anti-biofouling properties of PVDF membranes. *Chem. Eng. J.* **2021**, *411*, 128524. [CrossRef]

36. Yu, Y.; Pan, D.; Qiu, S.; Ren, L.; Huang, S.; Liu, R.; Wang, L.; Wang, H. Polyphenylene sulfide paper-based sensor modified by Eu-MOF for efficient detection of Fe^{3+}. *React. Funct. Polym.* **2021**, *165*, 104954. [CrossRef]

37. Firouzjaei, M.D.; Shamsabadi, A.A.; Sharifian Gh, M.; Rahimpour, A.; Soroush, M. A Novel Nanocomposite with Superior Antibacterial Activity: A Silver-Based Metal Organic Framework Embellished with Graphene Oxide. *Adv. Mater. Interfaces* **2018**, *5*, 1701365. [CrossRef]

38. Seyedpour, S.F.; Arabi Shamsabadi, A.; Khoshhal Salestan, S.; Dadashi Firouzjaei, M.; Sharifian Gh, M.; Rahimpour, A.; Akbari Afkhami, F.; Shirzad Kebria, M.R.; Elliott, M.A.; Tiraferri, A.; et al. Tailoring the Biocidal Activity of Novel Silver-Based Metal Azolate Frameworks. *ACS Sustain. Chem. Eng.* **2020**, *8*, 7588–7599. [CrossRef]

39. Zhang, M.; Wang, G.; Wang, D.; Zheng, Y.; Li, Y.; Meng, W.; Zhang, X.; Du, F.; Lee, S. Ag@MOF-loaded chitosan nanoparticle and polyvinyl alcohol/sodium alginate/chitosan bilayer dressing for wound healing applications. *Int. J. Biol. Macromol.* **2021**, *175*, 481–494. [CrossRef]

40. Liu, N.; Zhang, J.; Wang, Y.; Zhu, Q.; Wang, C.; Zhang, X.; Duan, J.; Hou, B.; Sheng, J. Combination of metal-organic framework with Ag-based semiconductor enhanced photocatalytic antibacterial performance under visible-light. *Colloids Surf. A Physicochem. Eng. Asp.* **2022**, *644*, 128813. [CrossRef]

41. Tang, J.; Chen, Y.; Zhao, M.; Wang, S.; Zhang, L. Phenylthiosemicarbazide-functionalized UiO-66-NH$_2$ as highly efficient adsorbent for the selective removal of lead from aqueous solutions. *J. Hazard. Mater.* **2021**, *413*, 125278. [CrossRef] [PubMed]

42. Prakash Tripathy, S.; Subudhi, S.; Das, S.; Kumar Ghosh, M.; Das, M.; Acharya, R.; Acharya, R.; Parida, K. Hydrolytically stable citrate capped Fe_3O_4@UiO-66-NH$_2$ MOF: A hetero-structure composite with enhanced activity towards Cr (VI) adsorption and photocatalytic H2 evolution. *J. Colloid Interface Sci.* **2022**, *606*, 353–366. [CrossRef]

43. Ruan, W.; Liu, H.; Wu, H.; Qi, Y.; Zhou, M.; Zhou, C.; Zhang, Z.; Yang, H. Fabrication of Uio-66-NH₂ with 4,6-Diamino-2-mercaptopyrimidine facilitate the removal of Pb2+ in aqueous medium: Nitrogen and sulfur act as the main adsorption sites. *Fuel Process. Technol.* **2022**, *236*, 107431. [CrossRef]

44. Hu, S.-z.; Huang, T.; Zhang, N.; Hu, S.; Lei, Y.-z.; Wang, Y. Enhanced removal of lead ions and methyl orange from wastewater using polyethyleneimine grafted UiO-66-NH₂ nanoparticles. *Sep. Purif. Technol.* **2022**, *297*, 121470. [CrossRef]

45. Guo, J.; Fan, X.; Wang, J.; Yu, S.; Laipan, M.; Ren, X.; Zhang, C.; Zhang, L.; Li, Y. Highly efficient and selective recovery of Au(III) from aqueous solution by bisthiourea immobilized UiO-66-NH₂: Performance and mechanisms. *Chem. Eng. J.* **2021**, *425*, 130588. [CrossRef]

46. Awad, F.S.; Bakry, A.M.; Ibrahim, A.A.; Lin, A.; El-Shall, M.S. Thiol- and Amine-Incorporated UIO-66-NH₂ as an Efficient Adsorbent for the Removal of Mercury(II) and Phosphate Ions from Aqueous Solutions. *Ind. Eng. Chem. Res.* **2021**, *60*, 12675–12688. [CrossRef]

47. Afridi, M.N.; Kim, J.-O. Statistical optimization of Mg-doped UiO-66-NH₂ synthesis for resource recovery from wastewater using response surface methodology. *Appl. Surf. Sci.* **2022**, *606*, 154973. [CrossRef]

48. Wang, Y.L.; Peñas-Garzón, M.; Rodriguez, J.J.; Bedia, J.; Belver, C. Enhanced photodegradation of acetaminophen over Sr@TiO2/UiO-66-NH₂ heterostructures under solar light irradiation. *Chem. Eng. J.* **2022**, *446*, 137229. [CrossRef]

49. Hu, Y.; Hu, B.; Ge, Y.; Nie, P.; Yang, J.; Huang, M.; Liu, J. In-situ synthesis of UiO-66-NH₂ on porous carbon nanofibers for high performance defluoridation by capacitive deionization. *Colloids Surf. A Physicochem. Eng. Asp.* **2022**, *646*, 129020. [CrossRef]

50. Zhang, W.; Shi, W.; Ji, W.; Wu, H.; Gu, Z.; Wang, P.; Li, X.; Qin, P.; Zhang, J.; Fan, Y.; et al. Microenvironment of MOF Channel Coordination with Pt NPs for Selective Hydrogenation of Unsaturated Aldehydes. *ACS Catal.* **2020**, *10*, 5805–5813. [CrossRef]

51. Taheri, M.; Ashok, D.; Sen, T.; Enge, T.G.; Verma, N.K.; Tricoli, A.; Lowe, A.; Nisbet, D.R.; Tsuzuki, T. Stability of ZIF-8 nanopowders in bacterial culture media and its implication for antibacterial properties. *Chem. Eng. J.* **2021**, *413*, 127511. [CrossRef]

52. Yang, S.A.; Choi, S.; Jeon, S.M.; Yu, J. Silica nanoparticle stability in biological media revisited. *Sci. Rep.* **2018**, *8*, 185. [CrossRef] [PubMed]

53. Chinnasamy, G.; Chandrasekharan, S.; Koh, T.W.; Bhatnagar, S. Synthesis, Characterization, Antibacterial and Wound Healing Efficacy of Silver Nanoparticles From Azadirachta indica. *Front. Microbiol.* **2021**, *12*, 611560. [CrossRef] [PubMed]

54. Chinnasamy, G.; Chandrasekharan, S.; Bhatnagar, S. Biosynthesis of Silver Nanoparticles from Melia azedarach: Enhancement of Antibacterial, Wound Healing, Antidiabetic and Antioxidant Activities. *Int. J. Nanomed.* **2019**, *14*, 9823–9836. [CrossRef]

55. Zhang, J.; Hu, Y.; Qin, J.; Yang, Z.; Fu, M. TiO₂-UiO-66-NH₂ nanocomposites as efficient photocatalysts for the oxidation of VOCs. *Chem. Eng. J.* **2020**, *385*, 123814. [CrossRef]

56. Wang, K.; Gu, J.; Yin, N. Efficient Removal of Pb(II) and Cd(II) Using NH2-Functionalized Zr-MOFs via Rapid Microwave-Promoted Synthesis. *Ind. Eng. Chem. Res.* **2017**, *56*, 1880–1887. [CrossRef]

57. Zhang, W.; Wang, L.; Zhang, J. Preparation of Ag/UiO-66-NH₂ and its application in photocatalytic reduction of Cr(VI) under visible light. *Res. Chem. Intermed.* **2019**, *45*, 4801–4811. [CrossRef]

58. Duan, S.; Xu, X.; Liu, X.; Wang, Y.; Hayat, T.; Alsaedi, A.; Meng, Y.; Li, J. Highly enhanced adsorption performance of U(VI) by non-thermal plasma modified magnetic Fe₃O₄ nanoparticles. *J. Colloid Interface Sci.* **2018**, *513*, 92–103. [CrossRef]

59. Cao, Y.; Zhao, Y.; Lv, Z.; Song, F.; Zhong, Q. Preparation and enhanced CO₂ adsorption capacity of UiO-66/graphene oxide composites. *J. Ind. Eng. Chem.* **2015**, *27*, 102–107. [CrossRef]

60. Firouzjaei, M.D.; Shamsabadi, A.A.; Aktij, S.A.; Seyedpour, S.F.; Sharifian Gh, M.; Rahimpour, A.; Esfahani, M.R.; Ulbricht, M.; Soroush, M. Exploiting Synergetic Effects of Graphene Oxide and a Silver-Based Metal-Organic Framework to Enhance Antifouling and Anti-Biofouling Properties of Thin-Film Nanocomposite Membranes. *ACS Appl. Mater. Interfaces* **2018**, *10*, 42967–42978. [CrossRef]

61. Zhang, Y.; Sun, P.; Zhang, L.; Wang, Z.; Wang, F.; Dong, K.; Liu, Z.; Ren, J.; Qu, X. Silver-Infused Porphyrinic Metal-Organic Framework: Surface-Adaptive, On-Demand Nanoplatform for Synergistic Bacteria Killing and Wound Disinfection. *Adv. Funct. Mater.* **2019**, *29*, 1808594. [CrossRef]

62. Yan, X.; He, B.; Liu, L.; Qu, G.; Shi, J.; Hu, L.; Jiang, G. Antibacterial mechanism of silver nanoparticles in Pseudomonas aeruginosa: Proteomics approach. *Metallomics* **2018**, *10*, 557–564. [CrossRef] [PubMed]